Homoepitaxial growth of $(\bar{1}02)$ β-Ga_2O_3 by halide vapor phase epitaxy

Yuichi Oshima* and Takayoshi Oshima

Research Center for Electronic and Optical Materials, National Institute for Materials Science, Tsukuba, Ibaraki 305-0044, Japan
E-mail: OSHIMA.Yuichi@nims.go.jp

Abstract

We demonstrated halide vapor phase epitaxy of β-Ga_2O_3 on a native $(\bar{1}02)$ substrate, which should be scalable and useful for the formation of vertical fins and trenches with smooth (100)-faceted sidewalls using plasma-free microfabrication techniques, e.g., selective area growth and gas etching, for use in power device applications. No misoriented domains were detected in the epiwafer during X-ray pole figure measurements. The full width at half maximum values of the X-ray rocking curves of the epiwafer were virtually the same as those of the bare substrate. No domain boundaries were found using scanning transmission electron microscopy at the film/substrate interface. The growth rate was as high as 23 μm/h, which was comparable to the rate for a (001) epilayer that was grown simultaneously.

Keywords: Ga_2O_3, HVPE, trench, fin

Introduction

Monoclinic-structured β-Ga_2O_3 is an oxide semiconductor that has an ultra-wide bandgap of E_g = 4.5 – 4.9 eV [1,2]. The critical field of this oxide should therefore be large and high-performance power devices with high breakdown voltages and low on-resistances can be expected when using this material [3,4]. In addition, bulk single crystal of β-Ga_2O_3 can be grown from the melt [5-11]. This is a great advantage against other wide-bandgap semiconductors such as GaN and SiC. However, the wafering of single crystalline β-Ga_2O_3 was believed to be impossible at the early stage of the development because of the serious cracking. Víllora et al found that the cracking can be suppressed by decreasing the density of twin boundaries, and demonstrated the successful wafering of 1-inch diameter β-Ga_2O_3 wafers [12]. Nowadays melt-grown high-quality β-Ga_2O_3 substrates up to 4 inches are commercially available, and high-quality epilayers can be grown on the native substrates without being suffered from lattice mismatch and resulting defects when an appropriate plane is selected. These features make β-Ga_2O_3 an attractive candidate material for future power device applications, and promising device prototypes including Schottky barrier diodes (SBDs) [13-16], heterojunction p-n diodes [4,17], modulation-doped field-effect transistors (MODFETs) [18,19], and metal-oxide-semiconductor FETs (MOSFETs) [20-24] have been reported.

Use of a 3D structure for β-Ga_2O_3-based power devices, which are known as trench MOS-type SBDs (MOSSBDs) [15,16] or FinFETs [22-24], provides an effective way to improve the breakdown voltage or to enable normally-off operation. To date, the micron/submicron-scale trenches/fins in these devices have been fabricated by plasma-based etching methods such as reactive ion etching (RIE) in most cases [25]. However, RIE introduces plasma damage onto the processed surface. This plasma damage causes an increase in the on-resistance of MOSSBDs [26], a reduction in their effective channel mobility [27], and the occurrence of a large hysteresis loop in FinFETs [28].

As a result, plasma-free microfabrication techniques have been investigated [29-34]. Recently, plasma-free fabrication of the trench/fin structures by selective area growth or using a HCl gas etching technique has been reported [33,34]. The technique enabled fabrication of trenches/fins along the [010] direction with flat (100) sidewalls and excellent controllability on a (001) β-Ga_2O_3 substrate; this is particularly important for industrial applications because the (001) substrates are scalable using the edge-defined film-fed growth (EFG) method, and the production of large-diameter wafers (2–6 in.) has been demonstrated [6]. However, the fact that the trenches/fins were inclined from the substrate normal by approximately 13.7° was problematic.

To solve this problem, we propose use of $(\bar{1}02)$ β-Ga_2O_3 substrates. As illustrated in Fig. 1, the $(\bar{1}02)$ plane is inclined from the (001) plane by approximately 13.7°. Therefore, fabrication of vertical trenches/fins along the [010] direction should be possible on a $(\bar{1}02)$ β-Ga_2O_3 substrate by using selective area growth/etching processes. In addition, the $(\bar{1}02)$ β-Ga_2O_3 substrates should be scalable because the $(\bar{1}02)$ plane can be a principal plane of a single crystal ingot grown by the EFG method along the [010] direction, along with the case of the (001) plane. Furthermore, $(\bar{1}02)$ β-Ga_2O_3 substrates should be suitable for use in device production because most of the nano-voids in the material should be oriented parallel to the in-plane [010] direction [6] and thus would hardly be exposed on the surface in a manner similar to the (001) case.

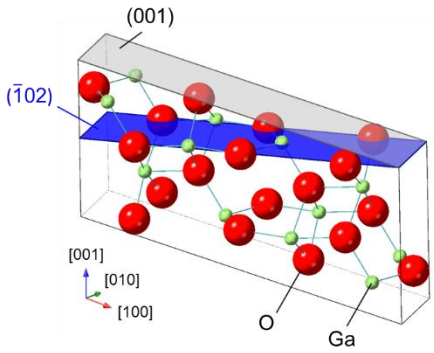

Figure 1. Crystal structure of β-Ga_2O_3.

The homoepitaxial growth behavior of β-Ga_2O_3 is highly anisotropic. The material's growth rate, surface morphology, and twinning characteristics are strongly dependent on the substrate orientation. For example, Sasaki *et al*. investigated growth rate anisotropy

in ozone molecular beam epitaxy and reported that the growth rate on the (100) plane was an order of magnitude smaller than the corresponding rates on the (001), (010), (101), and (310) planes [35]. Goto *et al*. performed a systematic investigation of the growth characteristics on crystal planes in the [100] zone from the (010) plane to the (001) plane by halide vapor phase epitaxy (HVPE) [36]. They reported that the growth rate was the lowest on the (010) plane and that the rate increased by a factor of approximately six in the vicinity of the (001) plane. Interestingly, a sharp drop in the (001) growth rate occurred when the miscut angle was smaller than 1°. The (001) surface showed a high density of pits and hillocks elongated along the [010] direction, while the (010) surface morphology was featureless. Furthermore, it has been reported that epitaxial growth on the (100) or $(\bar{2}01)$ planes causes serious twinning [37,38]. For the (100) plane, the density of the twin boundaries was strongly dependent on the miscut angle [37].

Consideration of the strong anisotropy described above indicates that the growth behavior on the $(\bar{1}02)$ plane should be investigated independently, although the angle of inclination from the well-investigated (001) plane is as small as 13.7°. Therefore, we examined a plain homoepitaxial $(\bar{1}02)$ β-Ga_2O_3 layer prior to the trial microfabrication of trench/fin structures by selective area growth/etching. The film was grown by HVPE because HVPE is advantageous for growth of the thick drift layer used in high-

breakdown-voltage devices because of the rapid growth rate.

Experimental

In this work, HVPE growth of β-Ga_2O_3 was performed in a laboratory-made quartz reactor at 1038°C and at atmospheric pressure using O_2 (>99.99995% pure) and GaCl as precursors. GaCl was synthesized upstream in the reactor via chemical reaction of Ga (>99.99999 pure) with HCl (>99.999% pure) at 822°C. HCl was also supplied into the growth zone to suppress parasitic reaction of the precursor materials [39]. The carrier gas was N_2 (dew point < −110°C). The gas species were supplied at vapor pressures of $P(O_2)/P(GaCl)/P(HCl)$ = 1.25/0.125/0.188 kPa for 5 min. We used a rectangular $(\bar{1}02)$ β-Ga_2O_3 substrate with dimensions of 10×15 mm^2. A (001) β-Ga_2O_3 substrate of the same dimensions was co-loaded for reference. Both substrates were manufactured by Novel Crystal Technology, Inc.

The surface morphology of the epilayers was characterized by Nomarski microscopy. The crystal orientation was examined via X-ray pole figure measurements. The crystal's mosaicity was estimated using X-ray rocking curve (XRC) measurements. $CuK_{\alpha 1}$ radiation (λ = 1.540562 Å) was used to perform the X-ray measurements. Secondary ion mass spectrometry (SIMS) was used to measure the residual impurity concentrations. The

coherence at the epilayer/substrate interface was examined by observing the atomic arrangement on the cross-section from the $[0\bar{1}0]$ direction using scanning transmission electron microscopy (STEM).

Results and discussion

Figure 2(a)–(c) and (d) show the surface morphologies of the $(\bar{1}02)$ epilayer and a $(\bar{1}02)$ substrate, respectively. The surface morphologies of the (001) epilayer and a (001) substrate are also shown for comparison in Fig. 2(e)–(g) and (h), respectively. The surface morphology of the both substrates were featureless. Hillock structures elongated along the [010] direction, which are typically observed for HVPE-grown (001) homoepitaxial films [40,41], appeared on both epilayers. The hillock density on the $(\bar{1}02)$ epilayer was higher than that on the (001) epilayer. Macro-steps along the [010] direction were observed between the hillocks on the $(\bar{1}02)$ epilayer, while the surface between the hillocks was featureless on the (001) epilayer. To identify the surface structure in detail, further investigation is necessary using other techniques such as atomic force microscopy and cross-sectional observations by scanning electron microscopy or transmission electron microscopy. The rougher morphology of the $(\bar{1}02)$ epilayer may indicate that the optimum growth conditions was different from those for the (001) epilayer. It is also likely that the surface condition of the $(\bar{1}02)$ substrate was worse than that of the (001)

substrate because the chemical mechanical polishing (CMP) conditions for the novel $(\bar{1}02)$ substrates should not be well-established compared to those for the well-investigated (001) substrates. Furthermore, the morphology may be sensitive to the miscut angle as well as the case for the (001) epilayers [41]. The growth/CMP conditions and miscut angle need to be optimized to discuss the intrinsic morphological differences. At present, the as-grown $(\bar{1}02)$ epilayer would not be smooth enough for use in device fabrication. The surface roughness should increase with increasing the thickness, and CMP to planarize the surface would be necessary as well as the case for the (001) epilayers; alternatively, better HVPE growth conditions including growth temperature, reactor pressure and VI/III ratio, should be investigated.

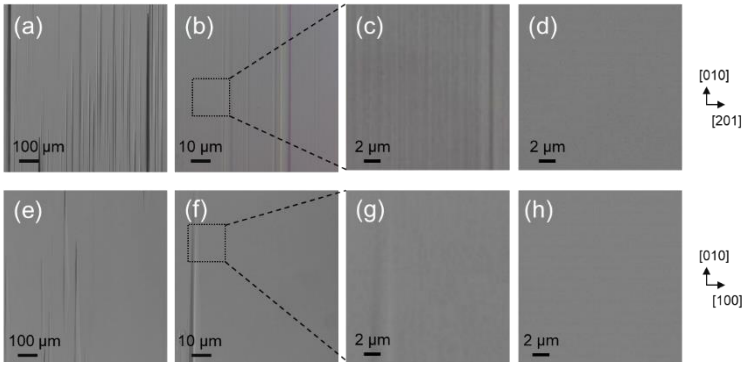

Figure 2. Nomarski microscopic images of (a)–(c) the $(\bar{1}02)$ epilayer, (d) a $(\bar{1}02)$ β-Ga_2O_3 substrate, (e)–(g) the (001) epilayer, and (h) a (001) β-Ga_2O_3 substrate.

Figure 3(a) and (b) show the X-ray pole figures of the $(\bar{1}02)$ epiwafer (χ = 0–86°). The

intensity is shown in log-scale in these figures. The pole figure in Fig. 3(a) was measured with 2θ for the 002 and $\bar{2}02$ diffractions (the 2θ values for these diffractions are virtually identical). The diffraction spots only appeared at the positions that were expected for single crystalline $(\bar{1}02)$ β-Ga_2O_3. However, this measurement cannot detect strongly misoriented domains (if any exist) with the (010) plane being close to parallel to the $(\bar{1}02)$ plane of the matrix, because the diffraction spots from the misoriented domains would appear beyond the measured χ range. Therefore, we also measured a pole figure with 2θ for the 111 and equivalent $1\bar{1}1$ diffractions (χ = 0°–86°), obtaining results as shown in Fig. 3(b). If the epilayer included misoriented domains of this type, the diffraction spots should appear around χ = 33°. However, the diffraction spots only appeared at the positions expected for single crystalline $(\bar{1}02)$ β-Ga_2O_3. We therefore concluded that the $(\bar{1}02)$ epilayer was a single crystalline layer.

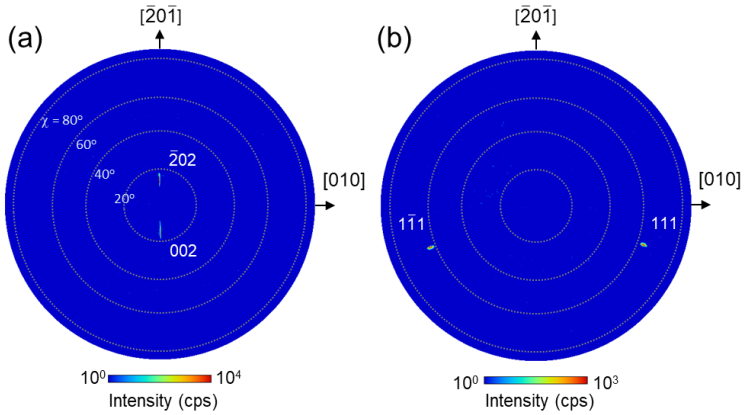

Figure 3. X-ray pole figures of the $(\bar{1}02)$ β-Ga_2O_3 epiwafer measured to detect the (a) 002 and $\bar{2}02$ diffractions, and the (b) 111 and $1\bar{1}1$ diffractions.

Figure 4(a) and (b) show the XRC profiles of the $\bar{2}04$ diffraction for the $(\bar{1}02)$ epiwafer when measured in symmetric geometry along the [010] and [$\bar{2}0\bar{1}$] directions, respectively. The full width at half maximum (FWHM) values should provide an indication of the tilting of the $(\bar{1}02)$ plane. XRC profiles for a $(\bar{1}02)$ bare substrate are also shown for comparison. The bare substrate was a different substrate to that used for the growth, but it was cut from the same β-Ga_2O_3 ingot. No significant differences were observed between the epiwafer and the bare substrate, irrespective of the measurement direction. The small sub-peaks originated from the substrate, because these sub-peaks were also observed for the bare substrate. Figure 4(c) shows an XRC profile of the $\bar{4}01$ diffraction when measured in skew-symmetric geometry (χ ~59.7°). The FWHM in this case should reflect the twisting around the [001] direction (surface normal axis). Once more, no significant differences were observed between the epiwafer and the bare substrate. Note that the XRC profiles include large contributions from the substrate because the film thickness was only 1.9 μm, as will be clarified later in this work. The contributions from the epilayer to the $\bar{2}04$ and $\bar{4}01$ peaks are estimated to be 19% and 57%, respectively; see the Appendix for the details of the calculation required. The results reported in this work should thus be confirmed using thicker films in future work. To increase the contribution from the epilayer to 99%, the film thicknesses must be 42 and 10 μm or more

for the $\bar{2}04$ and $\bar{4}01$ diffractions, respectively. These thicknesses should be accessible by rapid film growth (~23 μm/h in this work) using HVPE.

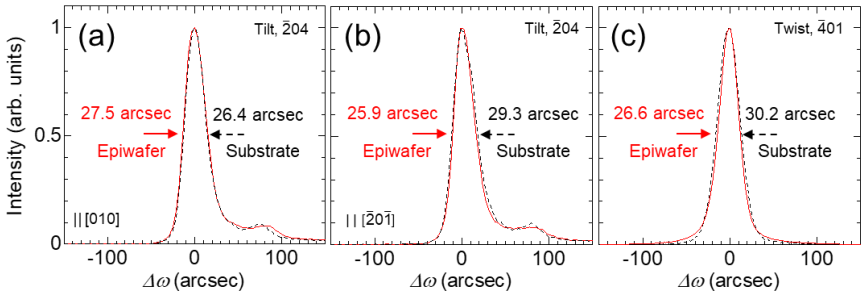

Figure 4. XRC profiles of the $(\bar{1}02)$ β-Ga_2O_3 epiwafer (red solid lines) and substrate (black dashed lines). (a) and (b) were measured for the $\bar{2}04$ diffraction in a symmetric geometry along the [010] and [$\bar{2}0\bar{1}$] directions, respectively. (c) was measured for the $\bar{4}01$ diffraction in a skew-symmetric geometry.

Table I summarizes the SIMS results for both the $(\bar{1}02)$ and (001) epilayers. With regard to [Si], no significant differences were observed between the two planes. Si is a donor impurity and [Si] should be reduced to 1×10^{16} cm^{-3} or less for use as the drift layer in a high-breakdown-voltage device. We believe that this reduction can be achieved by optimizing the growth conditions and the reactor design. [H] and [Cl], which are likely to have originated from GaCl and HCl, in the $(\bar{1}02)$ epilayer were twice and 1/4 of the corresponding quantities in the (001) epilayer, respectively. The concentration differences may reflect the difference in the microscopic surface structure including the density of dangling bonds, but the detailed mechanism is unclear at present. Both H and Cl were predicted theoretically to be shallow donors and should thus also be reduced.

Table I. Impurity concentrations in the β-Ga_2O_3 epilayers as estimated by SIMS. DL denotes the detection limit.

	[H] (cm^{-3})	[C] (cm^{-3})	[Si] (cm^{-3})	[Cl] (cm^{-3})
(-102)	1.2×10^{17}	< DL	2.7×10^{16}	6.3×10^{15}
(001)	6.4×10^{16}	< DL	2.6×10^{16}	2.7×10^{16}
DL	5×10^{16}	5×10^{16}	1×10^{15}	3×10^{14}

Based on the positioning of the Si spike at the interface between the epilayer and the substrate in the SIMS depth profile (not shown here), the $(\bar{1}02)$ film thickness was found to be 1.9 μm (corresponding to a growth rate of 23 μm/h). Similarly, the (001) film growth rate was 26 μm/h. The growth rate on the $(\bar{1}02)$ surface was slightly lower than that on the (001) surface, but was still high enough to grow a thick drift layer.

Figure 5(a) shows the selective area electron diffraction (SAED) pattern obtained from a cross-sectional area that included the film/substrate interface. The diffraction spots appeared only at the positions expected for the $(\bar{1}02)$-oriented single crystalline β-Ga_2O_3. Figure 5(b) shows a cross-sectional high-angle-annular-dark-field STEM (HAADF-

STEM) image in the vicinity of the film/substrate interface. No domain boundaries were found in this image, as expected from the SAED results. Figure 5(c) shows a magnified HAADF-STEM image of the film. White dots represent the Ga atoms that show the expected arrangement of the Ga sublattice for single crystalline $(\bar{1}02)$ β-Ga_2O_3, while the O atoms are not visible because their atomic number is much smaller than that of Ga. Therefore, we performed annular bright-field (ABF) STEM measurements of the same area simultaneously. The ABF-STEM method can visualize heavy elements and light elements simultaneously with a darker contrast for the heavier elements [42,43]. Figure 5(d) shows the corresponding ABF-STEM image. The Ga and O atoms are visible as black and gray dots, respectively. Their atomic arrangements coincided with those of the single crystalline $(\bar{1}02)$ β-Ga_2O_3.

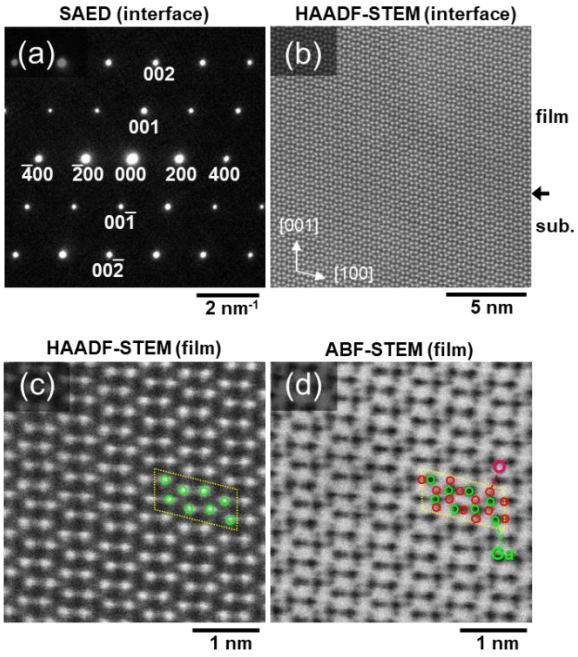

Figure 5. (a) SAED pattern obtained from an area that included the film/substrate interface. (b) HAADF-STEM image acquired in the vicinity of the interface (as indicated by the arrow). (c), (d) Magnified images of the film acquired by HAADF-STEM and ABF-STEM, respectively. Unit cells of β-Ga_2O_3 are shown to provide a clear understanding of the crystal orientation and the atomic arrangement. In all images, the upward direction represents the [001] growth direction, which is oriented perpendicular to the $(\bar{1}02)$ plane.

Summary

In summary, HVPE growth of $(\bar{1}02)$ β-Ga_2O_3 on a native substrate was demonstrated. The surface morphology of the $(\bar{1}02)$ epilayer showed hillock structures elongated along the [010] direction with a density that was greater than that on the (001) epilayer grown simultaneously. The $(\bar{1}02)$ epilayer growth rate was as high as 23 μm/h, which was comparable to that on the (001) plane. X-ray pole figure measurements detected no misoriented domains in the $(\bar{1}02)$ epilayer; this result was also verified by SAED and STEM images acquired at the film/substrate interface. The [Si] in the $(\bar{1}02)$ epilayer was

virtually the same as that found in the (001) film, while the [H] and [Cl] were twice and 1/4 of those in the (001) film, respectively. We believe the achievements of this study pave the way for the production of high-performance power devices with vertical fins/trenches fabricated through the plasma-free selective area growth/etching on scalable $(\bar{1}02)$ β-Ga_2O_3 substrates.

Acknowledgements

XRD measurements and STEM were performed using the open facility platform in the National Institute for Materials Science. This work was partially supported by the TEPCO Memorial Foundation.

Appendix

The penetration depth Z for X-rays in the symmetric reflection geometry is calculated as follows:

$$Z = K\frac{cos\chi sin\theta}{2\mu} \quad (1)$$

K is expressed using the film-to-bulk diffraction intensity ratio r as follows:

$$K = -\ln(1-r) \quad (2)$$

$\mu = 2.915\times10^2$ cm^{-1} is the linear attenuation coefficient of β-Ga_2O_3 for Cu $K_{\alpha1}$ radiation,

which is the product of the mass density of 5.9452 gcm^{-3} and the mass attenuation coefficient of 49.03 cm^2g^{-1} [44]. When Z is equal to the film thickness, the corresponding r value gives the contribution ratio from the film.

References

[1] M. Orita, H. Ohta, and M. Hirano, H. Hosono, Appl. Phys. Lett. **77**, 4166 (2000).

[2] T. Onuma, S. Saito, K. Sasaki, T. Masui, T. Yamaguchi, T. Honda and M. Higashiwaki, Jpn. J. Appl. Phys. 54 112601 (2015).

[3] M. Higashiwaki, G.H. Jessen, Appl. Phys. Lett. **112**, 060401 (2018).

[4] J. Zhang, P. Dong, K. Dang, Y. Zhang, Q. Yan, H. Xiang, J. Su, Z. Liu, M. Si, J. Gao, M. Kong, H. Zhou and Y. Hao, Nature Communications **13**, 3900 (2022).

[5] H. Aida, K. Nishiguchi, H. Takeda, N. Aota, K. Sunakawa, and Y. Yaguchi, Jpn. J. Appl. Phys. **47**, 8506–8509 (2008).

[6] A. Kuramata, K. Koshi, S. Watanabe and Y. Yamaoka: Galium oxide -Materials Properties, Crystal Growth, and Devices, Ed. By M. Higashiwaki and S. Fujita, Chapter 4 (Springer, 2020).

[7] K. Hoshikawa, T. Kobayashi, Y. Matsuki, E. Ohba, T. Kobayashi: J. Cryst. Growth **545**, 125724 (2020).

[8] K. Hoshikawa, T. Kobayashi, E. Ohba, T. Kobayashi, J. Cryst. Growth **546**, 125778

(2020).

[9] Y. Ueda, T. Igarashi, K. Koshi, S. Yamakoshi, K. Sasaki and A. Kuramata: Jpn. J. Appl. Phys. **62**, SF1006 (2023).

[10] Z. Galazka: J. Appl. Phys. **131**, 031103 (2022).

[11] J. D. Blevins, K. Stevens, A. Lindsey, G. Foundos, and L. Sande, IEEE TRANSACTIONS ON SEMICONDUCTOR MANUFACTURING **32**, 466 (2019).

[12] E. G. Víllora, K. Shimamura, Y. Yoshikawa, K. Aoki, N. Ishinose, J. Cryst. Growth **270**, 420 (2004).

[13] T. Oshima, T. Okuno, N. Arai, N. Suzuki, S. Ohira, and S. Fujita, Appl. Phys. Express **1**, 011202 (2008).

[14] P. Dong, J. Zhang, Q. Yan, Z. Liu, P. Ma, H. Zhou, and Y. Hao, IEEE Electron Device Lett. **43**, 765 (2022).

[15] K. Sasaki, D. Wakimoto, Q. T. Thieu, Y. Koishikawa, A. Kuramata, M. Higashiwaki, and S. Yamakoshi, IEEE Electron Device Lett. **38**, 783 (2017).

[16] F. Otsuka, H. Miyamoto, A. Takatsuka, S. Kunori, K. Sasaki, and A. Kuramata, Appl. Phys. Express **15**, 016501 (2022).

[17] Y. Kokubun, S. Kubo and S. Nakagomi, Appl. Phys. Express **9**, 091101 (2016).

[18] T. Oshima, Y. Kato, N. Kawano, A. Kuramata, S. Yamakoshi, S. Fujita, T. Oishi,

and M. Kasu, Appl. Phys. Express **10**, 035701 (2017).

[19] A. Vaidya, C. N. Saha, and U. Singisetti, IEEE Electron Device Lett. **42**, 1444 (2021).

[20] M. Higashiwaki, K. Sasaki, T. Kamimura, M. Hoi Wong, D. Krishnamurthy, A. Kuramata, T. Masui, and S. Yamakoshi, Appl. Phys. Lett. **103**, 123511 (2013).

[21] K. Zeng, R. Soman, Z. Bian, S. Jeong, and S. Chowdhury, IEEE Electron Device Lett. **43**, 1527 (2022).

[22] K. D. Chabak, N. Moser, A. J. Green, D. E. Walker, S. E. Tetlak, E. Heller, A. Crespo, R. Fitch, J. P. McCandless, K. Leedy, M. Baldini, G. Wagner, Z. Galazka, X. Li, and G. Jessen, Appl. Phys. Lett. **109**, 213501 (2016).

[23] W. Li, K. Nomoto, Z. Hu, T. Nakamura, D. Jena, and H. G. Xing, in IEEE International Electron Devices Meeting (IEEE, 2019), pp. 12.4.1−12.4.4.

[24] H. Huang, Z. Ren, AFM A. U. Bhuiyan, Z. Feng, Z. Yang, X. Luo, A. Q. Huang, A. Green, K. Chabak, H. Zhao, and X. Li, Appl. Phys. Lett. **121**, 052102 (2022).

[25] R. Khanna, K. Bevlin, D. Geerpuram, J. Yang, F. Ren, and S. Pearton, Gallium Oxide (Elsevier, 2019), pp. 263−285.

[26] W. Li, K. Nomoto, Z. Hu, D. Jena, and H. G. Xing, IEEE Electron Device Lett. **41**, 107 (2020).

[27] Z. Hu, K. Nomoto, W. Li, Z. Zhang, N. Tanen, Q. T. Thieu, K. Sasaki, A. Kuramata, T. Nakamura, D. Jena, and H. G. Xing, Appl. Phys. Lett. **113**, 122103 (2018).

[28] K. D. Chabak, N. Moser, A. J. Green, D. E. Walker, S. E. Tetlak, E. Heller, A. Crespo, R. Fitch, J. P. McCandless, K. Leedy, M. Baldini, G. Wagner, Z. Galazka, X. Li, and G. Jessen, Appl. Phys. Lett. **109**, 213501 (2016).

[29] Y. Yamazaki, M. Tomoaki, A. Takeki, and A. Kikuchi, in 4th International Workshop on Gallium Oxide and Related Materials, 2022.

[30] H. Huang, M. Kim, X. Zhan, K. Chabak, J. D. Kim, A. Kvit, D. Liu, Z. Ma, J. Zuo, and X. Li, ACS Nano **13**, 8784 (2019).

[31] Y. Oshima, E. Ahmadi, S. Kaun, F. Wu and J. S. Speck, Semicond. Sci. Technol. **33**, 015013 (2018).

[32] N. K. Kalaricka, A. Fiedler, S. Dhara, H. Huang, A F M A. U. Bhuiyan, M. W. Rahman, T. Kim, Z. Xia, Z. J. Eddine, A. Dheenan, M. Brenner, H. Zhao, J. Hwang, and S. Rajan, Appl. Phys. Lett. **119**, 123503 (2021).

[33] T. Oshima and Y. Oshima, Appl. Phys. Express **15**, 075503 (2022).

[34] T. Oshima and Y. Oshima, Appl. Phys. Lett. **122**, 162102 (2023).

[35] K. Sasaki, M. Higashiwaki, A. Kuramata, T. Masui, S. Yamakoshi, J. Cryst. Growth **378**, 591 (2013).

[36] K. Goto, H. Murakami, A. Kuramata, S. Yamakoshi, M. Higashiwaki, and Y. Kumagai, Appl. Phys. Lett. **120**, 102102 (2022).

[37] R. Schewski, M. Baldini, K. Irmscher, A. Fiedler, T. Markurt, B. Neuschulz, T. Remmele, T. Schulz, G. Wagner, Z. Galazka, and M. Albrecht, J. Appl. Phys. **120**, 225308 (2016).

[38] T. Ngo, D. Le, J. Lee, S. Hong, J. Ha, W. Lee, Y. Moon, J. Alloys and Compounds **834**, 155027 (2020).

[39] Y. Oshima, K. Kawara, T. Oshima, M. Okigawa, and T. Shinohe, Semicond. Sci. Technol. **35**, 055022 (2020).

[40] H. Murakami, K. Nomura, K. Goto, K. Sasaki, K. Kawara, Q. Thieu, R. Togashi, Y. Kumagai, M. Higashiwaki, A. Kuramata, S. Yamakoshi, B. Monemar, and A. Kokitu, Appl. Phys. Express **8**, 015503 (2015).

[41] C. Lin, K. Ema, S. Masuya, Q. Thieu, R. Sakaguchi, K. Sasaki, and A. Kuramata, Jpn. J. Appl. Phys **62**, SF1005 (2023).

[42] S. D. Findlay, N. Shibata, H. Sawada, E. Okunishi, Y. Kondo, T. Yamamoto, Y. Ikuhara, Ultramicroscopy **49**, 4 (1993).

[43] S. D. Findlay, N. Shibata, H. Sawada, E. Okunishi, Y. Kondo, Y. Ikuhara, Ultramicroscopy **110**, 903 (2010).

[44] M.J. Berger, J.H. Hubbell, S.M. Seltzer, J. Chang, J.S. Coursey, R. Sukumar, D.S. Zucker, and K. Olsen, XCOM: Photon Cross Sections Database version 1.5 (2010) (https://www.nist.gov/pml/xcom-photon-cross-sections-database).